American Mineralogist, Volume 94, pages 1216–1222, 2009

Mineral chemistry and alteration of rare earth element (REE) carbonates from alkaline pegmatites of Mount Malosa, Malawi

ALESSANDRO GUASTONI,[1] FABRIZIO NESTOLA,[1,2,*] AND AURELIO GIARETTA[2]

[1]Dipartimento di Geoscienze, Università di Padova, Via Giotto 1, I-35137, Padova, Italy
[2]Istituto di Geoscienze e Georisorse, CNR—Padova, Corso Garibaldi 37, 35137 Padova, Italy

ABSTRACT

In this study, the mineral chemistry and alteration of bastnäsite-(Ce), parisite-(Ce), and synchysite-(Ce) was investigated by EMPA, TG, DTG, CHNS, and SCXRD techniques. Relevant chemical data on light and volatile elements and X-ray diffraction data useful to evaluate the effect of OH content on the unit-cell volume of such carbonates are provided. Significant amounts of OH in both the parisite-(Ce) and synchysite-(Ce) were found, and these data are the first direct evidence of hydration for these carbonates. Single-crystal X-ray diffraction data showed that hydration causes an increase in the unit-cell volume for parisite and synchysite. Parisite-(Ce) and synchysite-(Ce) OH end-members have not been described in nature so far, and the amount of water must be taken into account for evaluating changes in stability field conditions. Textural relationships and replacement processes are discussed.

Keywords: Ca-REE carbonates, Mount Malosa, Malawi, hydration

INTRODUCTION

The crystal structures of bastnäsite-(Ce) and synchysite-(Ce), based on the old definition by Donnay and Donnay (1953), are the two end-members of the Ca-REE fluorocarbonate mineral series, however, they can be also considered as belonging to the bastnäsite-(Ce)–vaterite ($CaCO_3$, hexagonal) series; parisite-(Ce) [$CaCe_2F_2(CO_3)_3$] represents the intermediate-member structure type formed by the unit-layers of the two end-members, respectively, bastnäsite-(Ce), $CeFCO_3$ and synchysite-(Ce) $CeFCO_3 \cdot CaCO_3$ in the proportion of 1:1 as reported in Donnay and Donnay (1953). Further investigations on minerals of this series showed that they form mixed-layer compounds characterized by syntactic intergrowths, polytypism, superstructures, stacking faults, and twinning along the (0001) crystallographic plane. The structures of Ca-REE fluorocarbonate minerals have been investigated by high-resolution transmission electron microscopy (HRTEM) and several polytypes of the Ca-REE fluorocarbonate mineral series B_2S and $CaCe_3(CO_3)_4F_3$ [a mixed member between bastnäsite-(Ce) and parisite-(Ce)] have been previously described (Landuyt and Amelincks 1975; Wu et al. 1998; Meng et al. 2001, 2002).

This work reports the occurrence of bastnäsite-(Ce), (Ce,REE)(CO_3)(F,OH), parisite-(Ce), $Ca(Ce,REE)_2(CO_3)_3(F,OH)_2$, and synchysite-(Ce), $Ca(Ce,REE)(CO_3)_2(F,OH)$ within the cavities of the alkaline granite-syenite pegmatites of the Mount Malosa pluton in Malawi, associated with rhabdophane-(Ce), (Ce,La)$PO_4 \cdot nH_2O$, rhabdophane-(La), (La,Ce)$PO_4 \cdot nH_2O$, and cerianite-(Ce), CeO_2 that replaces bastnäsite-(Ce) and/or parisite-(Ce). Note that synchysite-(Ce), rhabdophane-(La), rhabdophane-(Ce), and cerianite-(Ce) have never been documented before in the pegmatites of Mount Malosa. The crystal chemistry of these Ca-REE fluorocarbonate minerals has been investigated by (1) electron-probe microanalyses (EPMA); (2) thermogravimetric (TG) and (3) differential thermogravimetric (DTG) profiles; (4) elemental (CHNS) (GC) analysis of total carbon and hydrogen; and (5) single-crystal X-ray diffraction.

EPMA, TG, and DTG analyses allowed us to quantify the contents of F, CO_2, and OH, as chemical data on light elements of Ca-REE fluorocarbonates are poorly represented in the literature and sometimes totally absent (Anthony et al. 2000).

The aim of this study is to describe the mineral assemblage of bastnäsite-(Ce), synchysite-(Ce), parisite-(Ce), rhabdophane-(Ce), rhabdophane-(La), and cerianite-(Ce), the textural relationships, and the replacement processes occurring among these Ca-REE fluorocarbonates. The common alterations observed at Mount Malosa are goethite + K-feldspar after parisite-(Ce), rhabdophane-(Ce) + bastnäsite-(Ce) + cerianite-(Ce) after parisite-(Ce), rhabdophane-(Ce) + rhabdophane-(La) after parisite-(Ce), and illite after bastnäsite-(Ce). Aggressive late-stage hydrothermal alkaline fluids are responsible for partial to complete replacement that affects Ca-REE-carbonates in the pegmatitic cavities at Mount Malosa. Elsewhere replacements after REE-carbonates have already been observed in alkaline and agpaitic pegmatites: for example at Lovozero Massif (Pekov 2000), Khibiny Massif (Yakovenchuk et al. 2005), and at Mount Saint Hilaire (Horváth and Gault 1990). To address the strong enrichment of Ca-REE fluorocarbonate in alkaline pegmatites of Mount Malosa this work also relates the role of complexing agents that allowed the transport of REE in hydrothermal fluids, and the geochemistry of magmatic sources responsible for enrichment of light rare-earth elements (LREE) and high field-strength elements (HFSE) represented by Nb, Zr, and Ti in alkaline pegmatites of Mount Malosa.

* E-mail: fabrizio.nestola@unipd.it

0003-004X/09/0809–1216$05.00/DOI: 10.2138/am.2009.3185

GEOLOGIC SETTING

The Zomba-Malosa pear-shaped pluton, emplaced approximately 113 ± 4 Ma (Eby et al. 1995) is composed of a central core of syenite and quartz-syenite, an inner ring of quartz-microsyenite, and an outer ring of peralkaline granite (Bloomfield 1965). This classic A-type anorogenic granitic suite belongs to the Chilwa-alkaline belt of Cretaceous age, which includes several smaller Cretaceous plutons composed of nepheline syenite, sodalite syenite, and carbonatites cropping out along the East African Mesozoic rift (Woolley 1987). All these plutons are related to the Chilwa Alkaline Province of Southern Malawi, and they intruded at shallow depths. In particular, the Zomba-Malosa pluton, based on closely spaced K-Ar amphibole, zircon, and apatite fission-track ages yielded a very rapid uplift rate and unroofing with respect to all the other plutons cropping out in this area (Eby et al. 1995). The associated miarolitic, granitic, and alkaline pegmatites of the Zomba-Malosa pluton are characterized by a unique mineralogy including: albite, aegirine, arfvedsonite, cerian-pyrochlore, fluorite, hingganite-(Y), microcline, several Nb-Ta-Y oxides, and Be-Na-Y-Zr-Ba silicates [e.g., eudidymite, epididymite, barylite, gadolinite-(Y), zircon], niobophyllite-astrophyllite mineral series, quartz, REE-carbonates, and xenotime-(Y) (Guastoni et al. 2003). These pegmatites mostly crop out along the syenite facies of the Malosa intrusion; they show the geochemical signature of niobium-yttrium-fluorine (NYF) type (Martin and De Vito 2005), but are also highly enriched with beryllium-zirconium-light rare earth elements (Be-Zr-LREE). Pegmatites cropping out close to the summit of Mount Malosa (~2000 m.a.s.l.) are subhorizontal, strongly miarolitic and often contain large decimetric up to metric cavities. The rock textures and the mineral assemblage indicate that these alkaline pegmatites crystallized at shallow depth. Indeed, a very recent work performed on aegirine from Mount Malosa collected in the cavities indicates the crystallization occurred at ~1 kbar and at a temperature of 300–400 °C (Secco et al. 2007). Moreover, an investigation on fluid inclusions in quartz crystals collected in miarolitic cavities of Mount Malosa estimates entrapment pressure at 130 MPa (Zajacz et al. 2006).

EXPERIMENTAL METHODS

Seven different specimens (Table 1), which include five large idiomorphic (up to several centimeters in length) crystals of Ca-REE fluorocarbonates and two other REE-carbonate crystals, the latter partially or completely replaced by rhabdophane and microcline + goethite, were investigated. All the specimens were carefully selected to analyze the mineral assemblage, the textural relationships, and to perform the electron-probe microanalyses, TG, DTG, CHNS analyses, and single-crystal X-ray diffraction studies. Very particular care was used to avoid as much as possible any kind of contamination from other mineral phases associated within the same specimen while performing the thermogravimetric and the elemental (CHNS) analyses.

Backscattered electron images were performed using a JEOL 5610 LV SEM. The chemical compositions of Ca-REE fluorocarbonates, rhabdophane-(Ce), and rhabdophane-(La) were determined using a Cameca CAMEBAX SX50 electron microprobe operating in wavelength dispersive mode with a fine-focused beam (~1 μm diameter), an acceleration voltage of 20 kV and a beam current of 20 nA, with 10 s counting times for peaks and 5 s for background. X-ray counts were converted to oxide wt% using the PAP correction program supplied by CAMECA (Pochou and Pichoir 1985). Natural minerals, synthetic phases, pure metal standards, spectral lines, and analytical crystals utilized were: wollastonite (Si$K\alpha$, TAP), wollastonite (Ca$K\alpha$, PET), corundum (Al$K\alpha$, TAP), apatite (P$K\alpha$, TAP), fluorapatite (F$K\alpha$, TAP), Fe_2O_3 (Fe$K\alpha$, LiF), synthetic Zr-Y-REE-silicates (Y$L\alpha$, PET; Zr$L\alpha$, REE$L\alpha$, and Nd$L\beta$, LiF), and synthetic ThO_2 and UO_2 (Th$M\alpha$ and U$M\alpha$, PET). The concentration of F was determined using an empirical correction for the major interference of Ce$L\alpha$ with F$K\alpha$.

Unit-cell parameters were obtained by single-crystal X-ray diffraction using a STOE single-crystal diffractometer equipped with a CCD detector (Oxford Diffraction) with graphite monochromated Mo$K\alpha$ radiation in the range $5 \le 2\theta \le 85°$ using 1° ω scan with exposure times between 10 and 30 s. The sample-detector distance was 60 mm. The CrysAlis RED program (Oxford Diffraction) was used to determine the unit-cell parameters for the samples investigated.

In samples 3L [synchysite-(Ce)], 6D [parisite-(Ce)], 7C [bastnäsite-(Ce)], and 9A [bastnäsite-(Ce) + parisite-(Ce)], the CO_2 content was measured by thermogravimetric analysis (TGA) and differential thermogravimetric analysis (DTG) using a prototypal CNR instrument (IGG-CNR, Padua, Italy). A type S (Pt-10% Rh/Pt) thermocouple placed inside an electric furnace was used for temperature measurements. The methodology requires the samples of Ca-REE fluorocarbonate minerals to be pulverized (mass 500 mg, particle size <75 μm) and inserted into a platinum crucible, placed on quartz glass support interfaced to a Mettler Toledo AB104 electronic balance. The heating rate was 10 °C/min, in air, from room temperature (20 °C) to a maximum temperature of 1000 °C. In samples 3L, 6D, 7C, and 9A determination of total carbon and hydrogen was obtained by Elemental Analyzer (CHNS) using a CE-Instruments EA 1110 automatic elemental analyzer, equipped with an AS 200 autosampler and Mettler Toledo AT21 electronic balance, using about 2 mg of powdered sample. The instrument is a simultaneous carbon-hydrogen-nitrogen and sulfur analyzer based on the reliable dynamic flash combustion at 1800 °C and GC separation (He carrier gas) followed by thermal

TABLE 1. Sample description of hand-specimens of the phases investigated

Sample no.	REE-carbonates	Description
6D	parisite-(Ce)	30 × 20 mm² aggregate of millimetric, platy, yellow-brown, pseudo-hexagonal crystals of rimmed by a very thin submillimetric crust composed by cerianite-(Ce)
1N	parisite-(Ce)	Large, barrel-shaped crystal of yellow-brown 30 × 30 mm parisite-(Ce) partially replaced by rhabdophane-(Ce) + cerianite-(Ce) and associated with zircon and dark green prisms of aegirine
9A	parisite-(Ce) bastnäsite-(Ce)	Large prismatic crystals 50 × 20 mm composed of inner gemmy brown parisite-(Ce) embedded in an opaque crust composed of yellow-brown bastnäsite-(Ce) + rhabdophane-(Ce) + cerianite-(Ce); the crystal lies on a large prism of aegirine associated with smoky quartz and zircon
7C	bastnäsite-(Ce) parisite-(Ce)	Barrel-shaped crystal of 40 × 40 mm composed of a dominant gemmy brown portion of bastnäsite-(Ce) interlayered with yellow-brown opaque parisite-(Ce)
3L	synchysite-(Ce)	Millimetric platy pseudo-hexagonal, reddish vitreous crystals of synchysite-(Ce) with a core composed of Th-rich parisite-(Ce) and associated with fergusonite-(Y), epididymite, microcline, aegirine, and quartz
4I	rhabdophane-(Ce) rhabdophane-(La)	40 × 20 mm prismatic pseudo-hexagonal pale-brown, earthy, spongy, and porous crystal of ex-parisite-(Ce) replaced by rhabodphane-(Ce) + rhabodphane-(La) + cerianite-(Ce) and associated with fibrous dark green aegirine
10	replaced parisite	Large, barrel-shaped, brownish 60 × 50 mm crystal of former parisite-(Ce), spongy and porous, and replaced by goethite + microcline

conductivity detectors (TCD). The calibration standards for carbon and hydrogen were prepared from known amounts of sulfanilamide ($C_6H_8N_2O_2S$).

Results and discussion

Bastnäsite-(Ce)

The sample 9A shows in the outer portion of the crystal analyzed (Fig. 1) bastnäsite-(Ce), rhabdophane-(Ce) + zircon + cerianite-(Ce). Chemical analysis of bastnäsite-(Ce) reveals a rather homogeneous composition (Table 2).

Sample 7C is formed by dominant bastnäsite-(Ce) and subordinate parisite-(Ce); this latter shows steep and lobate margins due to the random orientation of the polished sample. Indeed, a thin section of sample 7C cut perpendicular to the *c* axis observed under polarized microscope reveals the textural relationships where thicker layers of bastnäsite-(Ce) are interlayered with thinner layers of parisite-(Ce) (Fig. 2). Both the Ca-REE fluorocarbonates are unaltered and replacement processes by rhabdophane or cerianite-(Ce) do not occur. Bastnäsite-(Ce) is chemically rather homogenous also in sample 7C (Table 2).

Parisite-(Ce)

BSE images of sample 6D show that the specimen is composed of layers of parisite-(Ce) having different gray tones likely due to slight compositional variations of Ca/REE ratios. The EPMA data for parisite-(Ce) of sample 6D is reported in Table 2.

The sample 9A shows an incipient process of replacement of bastnäsite-(Ce) + cerianite-(Ce) + rhabdophane-(Ce) after parisite-(Ce) as observed in backscattered electron images. Parisite-(Ce) (Fig. 1) is dominant toward the inner portion of the crystal, bastnäsite-(Ce) (Fig. 1) and rhabdophane-(Ce) replacements occur along the outer portion of the crystal (reticulated area in Fig. 1). Parisite-(Ce) in sample 9A shows no sensible variations in compositional ranges with respect to sample 6D (Table 2).

Due to the difficulty of separating enough material for analysis and to avoid contamination with interlayers of bastnäsite-(Ce), on sample 7C the TG, DTG, and GC analyses were not performed. The chemical analysis of parisite-(Ce) is not reported in Table 2; Ca content ranges from 9.25 to 9.88 wt% CaO; Ce from 28.07 to 29.24 wt% Ce_2O_3; La from 15.05 to 16.80 wt% La_2O_3; Nd from 6.88 to 8.76 wt% Nd_2O_3; Pr from 2.63 to 3.62 wt% Pr_2O_3; Sm from 1.82 to 2.40 wt% Sm_2O_3; Y from 1.41 to 1.68 wt% Y_2O_3; Th from 0.60 to 1.07 wt% ThO_2; and F content in the range from 8.0 to 8.25 wt%.

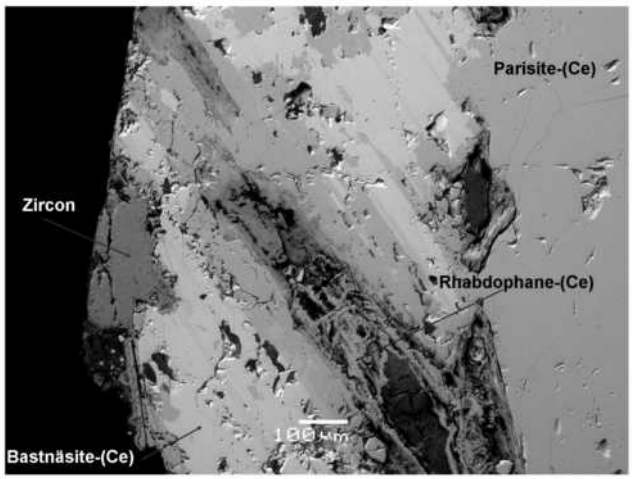

Figure 1. BSE image of sample 9A, with inner portion composed of parisite-(Ce) and outer portion of bastnäsite-(Ce). Rhabdophane-(Ce) occurs replacing parisite-(Ce).

In sample 1N, as well, TG, DTG, and GC were not performed because it was not possible to separate "uncontaminated" parisite-(Ce) from the rest of the crystal that is partially replaced by rhabdophane-(Ce) + cerianite-(Ce). EPMA data for parisite-(Ce) is not reported in Table 2; Ca ranges from 9.12 to 9.72 wt% CaO; Ce from 25.23 to 27.69 wt% Ce_2O_3; La from 9.70 to 11.79 wt% La_2O_3; Nd from 10.95 to 12.53 wt% Nd_2O_3; Pr from 2.75 to 3.76 wt% Pr_2O_3; Sm from 2.93 to 3.60 wt% Sm_2O_3; Y from 1.40 to 1.98 wt% Y_2O_3; Th from 0.50 to 0.74 wt% ThO_2; and F content in the range from 7.5 to 7.9 wt%.

Synchysite-(Ce)

Sample 3L is composed of synchysite-(Ce), and backscattered images reveal an inner portion of the crystal (Fig. 3) having a Th-rich parisite-(Ce) composition. BSE images show fergusonite-(Y) (Fig. 3) overgrown along the rim of the synchysite-(Ce) crystal. EMPA data for synchysite-(Ce) in sample 3L is reported in Table 2.

Replacements of Ca-REE-fluorocarbonates

Sample 4I is completely replaced by a reticulated net of prismatic crystals composed of rhabdophane-(Ce) + rhabdophane-(La) + cerianite-(Ce) (Fig. 4). Rhabdophane also lines secondary cavities forming fibrous crystals up to 20 µm in length with the cerianite-(Ce) occurring along the rims of the cavities (Fig. 4).

Sample 1N contains rhabdophane-(Ce) + parisite-(Ce) + cerianite-(Ce) + zircon. Backscattered electron images show prismatic fibrous aggregates of rhabdophane-(Ce) crystals lining secondary cavities with fibrous crystals up to 20 µm in length and replacing parisite-(Ce). The abundance of cavities in both specimens 4I and 1N posed serious problems in performing quantitative electron microprobe analysis. Rhabdophane contains a high concentration of water and tends to degrade under the beam of the electron microprobe. Chemical analyses reported in the literature do not match with the theoretical composition due to the ideal water content, which should be around 7.1 wt% H_2O (e.g., Anthony et al. 2000 and references therein). In samples 1N and 4I, the analyses of rhabdophane showed the water content considerably varies. These chemical data are confirmed by Vlasov et al. (1964), who reported water contents between 6.0 and 10.6 wt% and by Bowles and Morgan (1984) for rhabdophane-(Ce) from Cornwall containing 7.9 wt% H_2O. Electron microprobe analyses of sample 4I for rhabdophane-(Ce) and rhabdophane-(La) are shown in Table 2.

Sample 1N shows, along the outer portion of a parisite-(Ce) crystal, an incipient alteration to rhabdophane-(Ce) + cerianite-(Ce). The analysis of rhabdophane-(Ce) of sample 1N replacing parisite-(Ce) can be found in Table 2.

Sample 10 is composed of goethite + microcline after a Ca-REE fluorocarbonate, probably parisite-(Ce), judging from the crystal morphology. BSE images reveal that goethite and micro-

TABLE 2. Chemical analyses for the phases investigated

Sample no.	6D		9A		9A		7C		3L	
Mineral	parisite-(Ce)		parisite-(Ce)		bastnäsite-(Ce)		bastnäsite-(Ce)		synchysite-(Ce)	
	wt%	range	wt%	range	wt%	range	wt%	range	wt%	range
Na_2O	–	–	–	–	–	–	–	–	–	–
CaO	9.10	8.65–9.71	9.45	9.32–9.76	0.12	0.05–0.25	0.06	0.05–0.09	17.15	15.56–17.94
FeO	–	–	–	–	–	–	–	–	–	–
Y_2O_3	0.20	0.10–0.44	0.81	0.49–1.13	0.57	0.22–0.60	0.28	0.15–0.51	6.72	5.91–7.34
La_2O_3	17.39	16.18–19.22	15.70	14.79–17.02	19.41	17.19–20.51	23.22	21.32–24.05	11.07	9.74–12.15
Ce_2O_3	32.22	31.07–33.26	30.88	30.38–32.29	36.19	34.38–36.95	37.31	36.04–37.98	21.33	20.95–22.79
Pr_2O_3	2.71	2.12–3.15	2.93	2.53–3.51	3.47	3.12–3.59	2.71	2.50–3.45	2.26	1.89–2.63
Nd_2O_3	7.27	6.25–8.08	8.36	7.76–8.88	9.17	8.81–9.53	6.74	6.30–7.32	6.93	6.28–7.58
Sm_2O_3	0.86	0.46–1.16	1.44	1.28–1.66	1.92	1.56–2.08	0.74	0.52-0.89	1.79	1.52–2.09
ThO_2	–	–	0.10	0.07–0.15	–	–	0.12	0.05–0.15	0.65	0.44–1.08
UO_2	–	–	–	–	–	–	–		–	–
CO_2	23.64	23.55–23.75	24.35	23.90–24.70	21.09	20.90–21.20	20.10	19.90–20.50	26.54	26.35–27.10
F	6.05	5.15–6.45	5.90	5.60–6.30	6.96	6.55–7.20	8.07	8.00–8.23	4.64	4.13–4.96
H_2O	0.38	0.20–0.45	0.50	0.30–0.60	0.80	0.70–0.95	0.30	0.20–0.45	0.57	0.50–0.64
Sum	99.82		100.42		99.70		99.65		99.65	
$F_2 = O^-$	–2.55		–2.48		–2.93		–3.40		–1.95	
Total	97.27		97.94		96.77		96.25		97.70	
	Ionic formula based on 11 Oatoms				**Ionic formula based on 4 O atoms**				**Ionic formula based on 7 O atoms**	
Ca apfu	0.91		0.92		–		–		0.99	
Y	0.01		0.04		0.01		0.01		0.19	
La	0.60		0.53		0.26		0.32		0.22	
Ce	1.10		1.03		0.48		0.51		0.42	
Pr	0.09		0.10		0.05		0.04		0.04	
Nd	0.24		0.27		0.12		0.09		0.13	
Sm	0.03		0.04		0.02		0.01		0.03	
Th	–		–		–		–		0.01	
Σ cations	2.98		2.93		0.94		0.98		2.03	
F	1.78		1.70		0.80		0.95		0.79	
OH	0.24		0.30		0.19		0.07		0.21	
Σ anions	2.02		2.00		0.99		1.02		1.00	

Sample no.	4I		4I		1N	
Mineral	rhabdophane-(La)		rhabdophane-(Ce)		rhabdophane-(Ce)	
	wt%	range	wt%	range	wt%	range
CaO	2.30	2.30–3.46	3.46	1.77–3.46	2.60	1.51–3.47
Fe_2O_3	0.35	0.10–0.35	0.10	0.10–0.25	–	–
Y_2O_3	1.22	0.90–1.22	0.90	0.51–0.90	2.04	1.21–2.16
La_2O_3	24.81	16.93–24.81	20.46	16.93–20.46	12.29	9.81–15.65
Ce_2O_3	4.53	4.53–21.94	21.94	21.94–27.47	28.28	16.24–28.68
Pr_2O_3	6.40	4.35–6.40	4.35	3.50–4.35	4.02	3.42–4.28
Nd_2O_3	18.80	11.64–18.80	11.64	9.96–11.64	13.24	11.82–17.90
Sm_2O_3	2.53	1.56–2.53	1.56	1.56–1.86	3.57	3.38–4.28
ThO_2	0.30	0.10–0.30	0.36	0.36–1.09	0.92	0.16–0.92
SiO_2	0.20	0.17–0.20	0.24	0.24–0.32	0.24	0.21–0.27
P_2O_5	25.71	25.50–25.71	26.51	25.40–26.51	27.33	25.46–27.55
Total	87.15		91.52		94.53	
	Ionic formula based on 16 O atoms					
Ca apfu	0.44		0.63		0.46	
Fe	0.05		0.01		–	
Y	0.12		0.08		0.18	
La	1.63		1.28		0.75	
Ce	0.30		1.37		1.71	
Pr	0.42		0.27		0.24	
Nd	1.20		0.71		0.78	
Sm	0.16		0.09		0.20	
Th	0.01		0.01		0.04	
Si	0.04		0.04		0.04	
P	3.88		3.82		3.83	
Σ cations	8.25		8.31		8.23	

cline (Fig. 5) have completely replaced the parent crystal. Textural relationships also evidence that goethite replaces microcline, and this process mainly occurs at the core of microcline crystals and diffuses outward. Sample 10 reveals mineral replacements or pseudomorphism reactions by dissolution/reprecipitation: the shape and the volume of the former parisite parent crystal is preserved revealing that the rate of dissolution of the parent equals the rate of precipitation of rhabdophane + cerianite-(Ce) and goethite + microcline (Putnis 2002).

Single-crystal X-ray diffraction

Four samples were suitable for single-crystal X-ray diffraction analysis. In particular, we have investigated samples 6D, 9A, 7C, and 3L. Unit-cell parameters for these samples are reported in Table 3. Samples 6D and 9A are two parisite-(Ce) crystals showing significant differences in unit-cell volume, with the volume of sample 9A being about 1.1% larger than that of sample 6D. No data concerning OH has been reported so far in the literature for parisite, therefore we do not have any data about

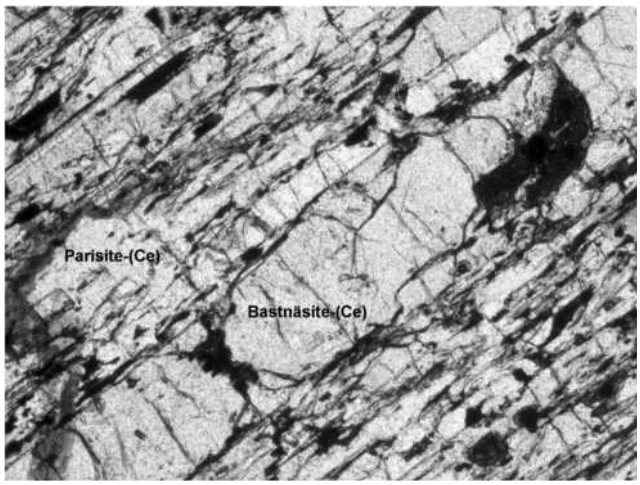

FIGURE 2. Thin section of sample 7C cut perpendicular to the *c* axis and observed by polarizing microscope.

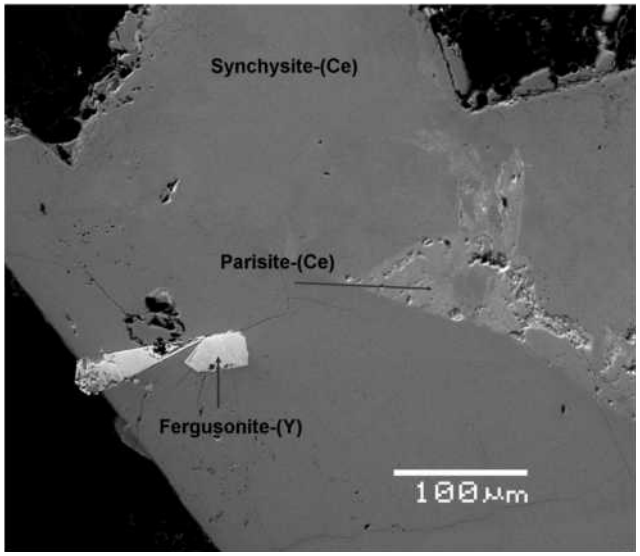

FIGURE 3. BSE image of sample 3L. It shows that synchysite-(Ce) has a core composed of Th-rich parisite-(Ce) (lighter gray).

TABLE 3. Unit-cell parameters for the samples studied in this work

Sample	6D Parisite-(Ce)	9A Parisite-(Ce)	7C Bastnäsite-(Ce)	3L Synchysite-(Ce)
a (Å)	12.323(2)	12.337(3)	7.110(1)	12.255(1)
b (Å)	7.1182(7)	7.126(1)	–	7.080(1)
c (Å)	28.261(3)	28.504(8)	9.771(2)	18.655(3)
β (°)	98.446(9)	98.29(2)	–	102.68(2)
V (Å^3)	2452.12	2479.70	427.77	1579.13
Space group	*Cc*	*Cc*	$P\bar{6}2c$	*C*2/*c*

the effect of OH on the unit-cell parameters of such phases and on their density. If we compare data for parisite-(Ce) published by Ni et al. (2000) with our samples 9A and 6D, it appears evident that the unit-cell volume increases with increasing OH content (sample 9A has OH content 22% higher than sample 6D). Considering that at the Ca and REE sites the mean cation radius does not show significant differences among the three samples, and that on some nominally anhydrous silicates (e.g., α-olivine, β-olivine, γ-olivine; Smyth et al. 2006 and references therein) the OH causes an increase in the unit-cell volume, we are confident

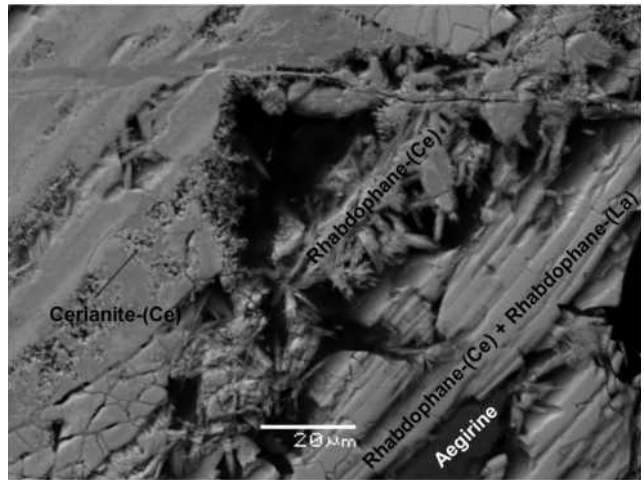

FIGURE 4. BSE image of sample 4I. Fibrous crystals of rhabdophane-(Ce) growing in a cavity lined with cerianite-(Ce). On the lower right side of the image is an intergrowth of rhabdophane-(Ce) and rhabdophane-(La).

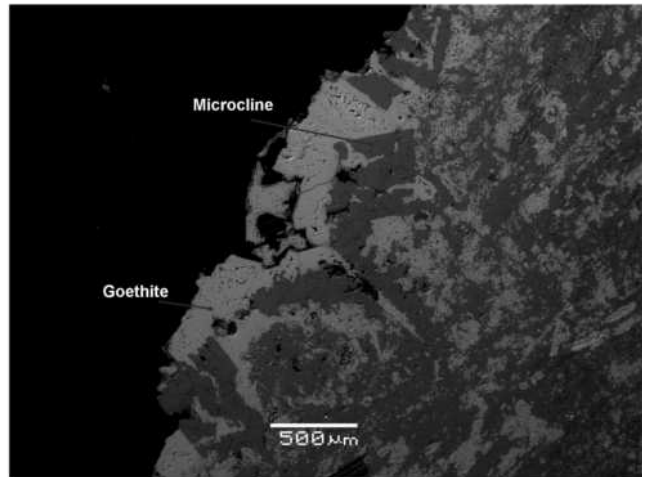

FIGURE 5. BSE image of sample 10. The image shows that goethite (light gray) and microcline (dark gray) have completely replaced the parent crystal, which was likely parisite-(Ce).

that OH in parisite could be the cause of the larger volume we found for sample 9A with respect to 6D one and the parisite-(Ce) of Ni et al. (2000). For the sample in Ni et al. (2000), the bond valence sum well demonstrates that no OH group is present in this parisite structure.

The unit-cell parameters of bastnäsite-(Ce) sample 7C studied in this work can be compared with that of bastnäsite-(Ce) by Ni et al. (1993). In this case, we found a practically identical unit-cell volume (almost negligible difference of about 0.1%). This appears to be in agreement with an extremely similar composition between the two samples. Our 7C sample however shows 0.07 pfu of OH, which we consider too low a content to justify any possible differences between the two samples here compared. As for parisite-(Ce) of Ni et al. (2000), the bastnäsite-(Ce) of Ni et al. (1993) shows that bond valence sums indicates no OH group in the crystal structure.

The synchysite-(Ce) sample 3L studied in this work shows

the largest difference with literature data of our three minerals studied (i.e., synchysite, parisite, and bastnäsite). Our sample 3L shows a unit-cell volume about 1.5% lower than that of the synchysite-(Ce) of Wang et al. (1994). In our opinion, the difference in the volume cannot be ascribed to the differences in mean cationic radius at Ca and REE sites, but rather to the OH water content. In Wang et al. (1994), no OH was reported, however, they provide the following chemical formula $(Ce_{0.62}La_{0.32}Th_{0.01}Eu_{0.01})_{0.96}(Ca_{0.94}Y_{0.02})_{0.96}F_{0.64}C_{1.96}O_6$ in which 0.357 pfu F is missing. As we could experimentally determine the OH content, and for our 3L synchysite we have $F_{0.79}OH_{0.21}$ (Table 2), in our opinion the 0.357 pfu of F missing in Wang et al. (1994) is probably OH. This could easily explain the markedly lower unit-cell volume of our sample, which should contain 42% less OH than the specimen of Wang et al. (1994).

Mineral chemistry and stability of Ca-REE-fluorocarbonates

For all the samples reported in Tables 1 and 2, the light and volatile elements F, CO_2, and OH were carefully quantified. These data provide a complete chemical characterization of natural Ca-REE fluorocarbonates that generally have light and volatile elements poorly defined in the literature (Anthony et al. 2000). In particular, the measures performed by TG and DTG allowed us to quantify a significant OH content in bastnäsite-(Ce), parisite-(Ce), and synchysite-(Ce). Regarding the samples of bastnäsite-(Ce), the F/OH ratios reveal always a prevalence of fluorine, and this indicates that the F dominance of bastnäsite-(Ce) is always present at Mount Malosa. Indeed hydroxylbastnäsite-(Ce) with space group $P\overline{6}$ (Haschke 1975; Yang et al. 2008), is much more rare compared to bastnäsite-(Ce) with F dominance and space group $P\overline{6}2c$ (Ni et al. 1993). Hsu (1992) in his experimental work was not able to synthesize bastnäsite-(Ce) compositions with intermediate F/OH ratio due to the high degree of structural disorder. This author also experimentally modeled the breakdown and stability field of F-rich bastnäsite-(Ce), which is wider than that of hydroxylbastnäsite-(Ce) because F-rich bastnäsite-(Ce) has better structural affinity to form even if the environment is relatively low in F.

The formation of large crystals of Ca-REE fluorocarbonates in the pegmatitic cavities of alkaline pegmatites at Mount Malosa implies the mechanisms that govern REE transportation through hydrothermal solutions. Bandurkin (1961) published a pioneering work in REE studies, and he first attributed an important role to complex fluoride. Flynn and Burnham (1978) did measure an increase in the partitioning of REE between aqueous vapor and granitic melt in the presence of fluoride agents. The experiments clarified that if such fluoride activities and temperatures predominate, then the authors could state that REE are transported by fluoride-bearing hydrothermal fluids. Other experimental work applied to granitic melts were performed by Bilal and Langer (1987); these authors determined that the stability field of REE-fluoride complexes can reach 200 °C and found a strong increase of REE-fluoride stability with increasing temperature. Again, Wood (1990) investigated the stability fields of bastnäsite; he studied REE-complexing behavior at elevated temperatures considering the trivalent state of REE extended to 350 °C, and observing that the fluoride lanthanides are strongly complexed with increasing temperature following the reaction $REE^{3+} + F^- = [(REE)F]^{2+}$. Wood (1990) demonstrated that the competition of F^- and OH^- for the REE^{3+} is depicted in the form of log a_{F^-} vs. pH diagrams. These diagrams show that fluoride complexation is predicted to be stronger relative to hydrolysis as temperature increases up to 350 °C. Wood showed that a mitigating factor could be related to the buffering of F^- to low activities by the precipitation of topaz or fluorite. Hand specimens of centimetric corroded fluorite crystals have occasionally been found in the pegmatite cavities at Mount Malosa, but eventually if such conditions should apply in an environment where REE are in solution with pH < 7, fluoride complexes still predominate over hydroxide complexes.

Williams-Jones and Wood (1992) showed in petrogenetic grids for REE fluorocarbonates that the assemblage parisite + fluorite is stable to higher temperature than the assemblage bastnäsite + fluorite. Unfortunately, the authors do not provide quantitative determinations of the *P-T* conditions for natural systems and experimental phase equilibrium data. Considering the data obtained from this study, a comparison with the sample 9A shows that the outward incipient process of replacement by bastnäsite-(Ce) is probably due to the influx of high-temperature hydrothermal fluids. This could mean that bastnäsite-(Ce) can also be a typical secondary replacement product associated with cerianite-(Ce), and this looks confirmed by experiments of Hsu (1992) in which the addition of CaO causes a destabilization of bastnäsite following a reaction like $2CeCO_3F + CaO = CaF_2 + Ce_2O_3 + CO_2$. It is also noteworthy that Huang et al. (1986) has synthesized bastnäsite-(Ce) up to temperatures of 400–450 °C and pressure of 1 kbar. Below 400 °C, they always obtained bastnäsite-(Ce), and above, fluocerite + cerianite-(Ce).

Samples 4A and 1N reveal mineral replacement reactions occurring by dissolution-reprecipitation processes at constant volume. In particular, the formation of secondary REE-bearing phases like rhabdophane + cerianite-(Ce) would mean that parent primary phases become unstable during fluid interactions and undergo decomposition with remobilization of the lanthanides into newly formed minerals. Akers et al. (1993) defined the upper stability limit of rhabdophane at 200 °C as a product of alteration of monazite, but the chemical and crystallographic analyses did not show any monazite in the samples studied; thus the replacement of rhabdophane occurred directly at expenses of REE-carbonates. As indicated by the aforementioned reaction the formation of cerianite-(Ce) associated with rhabdophane occurred by effect of f_{O_2} due to the transition of Ce^{3+} to Ce^{4+}.

Very reactive hydrothermal fluids occurred in the pegmatite cavities hosting sample 10, causing complete transformation of a parent primary REE-carbonate (probably parisite) into a mixture of goethite + microcline, and such pseudomorphism reactions occurred maintaining a constant volume of the parent primary phase. It is not clear if replacement processes occurred during the crystallization of REE-carbonates in the cavities, or whether they may be related to a postmagmatic subsolidus process triggered by reaction of consolidated phases with hydrothermal alkaline fluids.

ACKNOWLEDGMENTS

We acknowledge Raoul Carampin of CNR-Padova for WDS electron microprobe facilities, Mario Picciani for REE-carbonates specimens utilized for this study, and Federico Pezzotta for electron microprobe facilities at the Museum of Natural

History of Milan. Herta Effenberger, an anonymous referee, and Artem Oganov are thanked for their helpful suggestions, which strongly improved this manuscript. Financial support has been provided by MIUR-PRIN 2006 to A. Dal Negro.

REFERENCES CITED

Akers, W.T., Grove, M., Harrison, T.M., and Ryerson, F.J. (1993) The instability of rhabdophane and its unimportance in monazite paragenesis. Chemical Geology, 110, 169–176.

Anthony, J.W., Bideaux, R.A., Bladh, K.W., and Nichols, M.C. (2000) Handbook of Mineralogy, IV, Phosphates, Arsenates, Vanadates. Mineral Data Publishing, Tucson, Arizona.

Bandurkin, G.A. (1961) Behavior of the rare earths in fluorine-bearing media. Geochemistry International, 2, 159–167.

Bilal, B.A. and Langer, P. (1987) Complex formation of trace elements in geochemical systems: stability constants of fluoro complexes of the lanthanides in a fluorite bearing model system up to 200 °C and 1000 bar. Inorganica Chimica Acta, 140, 297–298.

Bloomfield, K. (1965) The geology of the Zomba area. Bulletin Geological Survey Malawi, 16, 1–193.

Bowles, J.F.W. and Morgan, D.J. (1984) The composition of rhabdophane. Mineralogical Magazine, 48, 146–148.

Donnay, G. and Donnay, J.D.H. (1953) The crystallography of bastnäsite-(Ce), parisite-(Ce), roentgenite-(Ce), and synchysite-(Ce). American Mineralogist, 38, 932–963.

Eby, G.N., Roden-Tice, M., Krueger, H.L., Ewing, W., Faxon, E.H., and Woolley, A.R. (1995) Geochronology and cooling history of the northern part of the Chilwa alkaline province, Malawi. Journal of African Earth Science, 20, 275–288.

Flynn, R.T. and Burnham, C.W. (1978) An experimental determination of rare earth partition coefficients between a chloride containing vapour phase and silicate melts. Geochimica et Cosmochimica Acta, 42, 685–701.

Guastoni, A., Pezzotta, F., and Demartin, F. (2003) Le pegmatiti di Zomba-Malosa. Rivista Mineralogica Italiana, 27, 66–77.

Haschke, J.M. (1975) The lanthanum hydroxide fluoride carbonate system: The preparation of synthetic bastnäsite. Journal of Solid State Chemistry, 12, 115–121.

Horváth, L. and Gault, R.A. (1990) The mineralogy of Mont Saint Hilaire, Quebec. The Mineralogical Record, 21, 281–359.

Huang, S., Wang, Z., Zhang, A., and He, S. (1986) Experimental studies of the condition of formation of bastnaesite. Acta Mineralogica Sinica, 6, 157–160.

Hsu, L.C. (1992) Synthesis and stability of bastnaesites in a part of the system (Ce,La)-F-H-C-O. Mineralogy and Petrology, 47, 87–101.

Landuyt, J.V. and Amelincks, S. (1975) Multiple beam direct lattice imaging of new mixed-layer compound of the bastnaesite-synchysite series. American Mineralogist, 60, 315–318.

Martin, R.F. and De Vito, C. (2005) The patterns of enrichment in felsic pegmatites ultimately depend on tectonic setting. Canadian Mineralogist, 43, 2027–2048.

Meng, D.W., Wu, X.L., Mou, T., and Li, D.X. (2001) Microstructural investigation of new polytypes in parisite-(Ce) by high resolution electron microscopy. Canadian Mineralogist, 39, 1713–1724.

Meng, D., Wu, X., Hang, Y., and Meng, X. (2002) Polytypism and microstructures of the mixed-layer member B_2S, $CaCe_3(CO_3)_4F_3$ in the bastnaesite-(Ce)–synchysite-(Ce) series. Earth and Planetary Science Letters, 203, 817–828.

Ni, Y., Hughes, J.M., and Mariano, A.N. (1993) The atomic arrangement of bastnäsite-(Ce), $Ce(CO_3)F$, and structural elements of synchysite-(Ce), röntgenite-(Ce), and parisite-(Ce). American Mineralogist, 78, 415–418.

Ni, Y., Post, J.E., and Hughes, J.M. (2000) The crystal structure of parisite-(Ce), $Ce_2CaF_2(CO_3)$. American Mineralogist, 85, 251–258.

Pekov, I.V. (2000) Lovozero Massif—History, Pegmatites, Minerals. Ocean Pictures Ltd., Moscow.

Pouchou, J.L. and Pichoir, F. (1985) "PAP" (phi-rho-z) procedure for improved quantitative microanalysis. In J.T. Armstrong, Eds., Microbeam Analysis, p. 104–106. San Francisco Press, California.

Putnis, A. (2002) Mineral replacement reactions: from macroscopic observations to microscopic mechanisms. Mineralogical Magazine, 66, 689–708.

Secco, L., Guastoni, A., Nestola, F., Redhammer, G.J., and Dal Negro, A. (2007) Crystal chemistry of aegirine as indicator of *P-T* conditions. Mineralogical Magazine, 71, 249–255.

Smyth, J.R. (2006) Hydrogen in high pressure silicate and oxide mineral structures. In H. Keppler and J.R. Smyth, Eds., Water in Nominally Anhydrous Minerals, 62, p. 155–167. Reviews in Mineralogy and Geochemistry, Mineralogical Society of America and Geochemical Society, Chantilly, Virginia.

Smyth, J.R., Frost, D.J., Nestola, F., Holl, C.M., and Bromiley, G. (2006) Olivine hydration in the deep upper mantle: Effects of temperature and silica activity. Geophysical Research Letters, 33, L15301.

Vlasov, K.A. (1964) Geochemistry, mineralogy and genetic types of rare element deposits, p. 830. Mineralogy Of Rare Elements, Vol. II, Nauka, Labour Press, Moscow.

Wang, L., Ni, Y., Hughes, M., and Bayliss, P. (1994) The atomic arrangement of synchysite-(Ce), $CeCaF(CO_3)_2$. Canadian Mineralogist, 32, 865–871.

Williams-Jones, A.E. and Wood, S.A. (1992) A preliminary petrogenetic grid for REE flurocarbonates and associated minerals. Geochimica et Cosmochimica Acta, 56, 725–738

Wood, S.A. (1990) The aqueous geochemistry of the rare-earth elements and yttrium. Theoretical predictions of speciation in hydrothermal solutions to 350 °C at saturation water vapor pressure. Chemical Geology, 88, 99–125.

Woolley, A.R. (1987) Lithosphere metasomatism and the petrogenesis of the Chilwa Province of alkaline igneous rocks and carbonatites, Malawi. Journal of African Earth Science, 6, 891–898.

Wu, X.L., Meng, D.W., and Pan, Z.L. (1998) Transmission electron microscopic study of new, regular mixed-layer structures in calcium rare-earth fluorocarbonate minerals. Mineralogical Magazine, 62, 55–64.

Yakovenchuk, V., Ivanyuk, G., Pakhomovsky, Y., and Men'shikov, Y. (2005) Khibiny, p. 468. In F. Wall, Ed., Laplandia Minerals. Apatity, Russia.

Yang, H., Dembowski, R.F., Conrad, P.G., and Downs, R.T. (2008) Crystal structure and Raman spectrum of hydroxyl-bästnasite-(Ce), $CeCO_3(OH)$. American Mineralogist, 93, 698–701.

Zajacz, Z., Halter, W.E., Pettke, T., and Guillong, M. (2006) Determination of fluid/melt partition coefficients by LA-ICPMS analysis of co-existing fluid and silicate melt inclusions. 4th Swiss Geoscience Meeting, Bern, Abstract 05/27.

MANUSCRIPT RECEIVED DECEMBER 31, 2008
MANUSCRIPT ACCEPTED APRIL 16, 2009
MANUSCRIPT HANDLED BY ARTEM OGANOV